





Robust perpendicular magnetic anisotropy of $\text{Co}_3\text{Sn}_2\text{S}_2$ phase in sulfur deficient sputtered thin filmsJunichi Shiogai ^{1,*}, Junya Ikeda,¹ Kohei Fujiwara ¹, Takeshi Seki ^{1,2}, Koki Takanashi,^{1,2,3} and Atsushi Tsukazaki ^{1,2,3}¹*Institute for Materials Research, Tohoku University, Sendai 980-8577, Japan*²*Center for Spintronics Research Network (CSRN), Tohoku University, Sendai 980-8577, Japan*³*Center for Science and Innovation in Spintronics (CSIS), Core Research Cluster, Tohoku University, Sendai 980-8577, Japan*

(Received 31 July 2020; revised 20 November 2020; accepted 15 January 2021; published 9 February 2021)

Perpendicular magnetic anisotropy (PMA) in magnetic thin films is a fundamental key feature in the design of spintronic devices. As one of magnetic Weyl semimetals, $\text{Co}_3\text{Sn}_2\text{S}_2$ has been studied for its large anomalous Hall effect (AHE), uniaxial crystalline magnetic anisotropy, and half metallicity. In this study, we investigated the effect of off-stoichiometric composition on the PMA and AHE of $\text{Co}_3\text{Sn}_2\text{S}_x$ thin films fabricated by the sputtering technique. The prepared thin films have off-stoichiometric S compositions x of 1.54 (S poor) and 3.27 (S rich) as well as the nearly stoichiometric one of 2.02. In addition to the $\text{Co}_3\text{Sn}_2\text{S}_2$ phase, the segregated Co metal is found to contribute to the measured magnetization in the S-poor and S-rich films. The coercive field of perpendicular magnetization in all the films is much larger than that in the $\text{Co}_3\text{Sn}_2\text{S}_2$ bulk crystals despite the fact that effective perpendicular magnetic anisotropy constants (K_u^{eff}) between the prepared films are significantly different. In addition, the K_u^{eff} values of two samples with $x = 2.02$ and 2.22 are comparable to those of the bulk crystals. In contrast to the isotropic magnetization behavior in the S-rich film, the S-poor film holds the PMA feature. This result means that the PMA is more robust in the S-poor film than in the S-rich film. For the electrical transport properties, a large tangent of Hall angle of about 0.2 is observed for both the nearly stoichiometric and the S-poor films. This large tangent of Hall angle demonstrates that the Weyl feature of $\text{Co}_3\text{Sn}_2\text{S}_2$ phase is well maintained even in the S-poor thin films as well as the nearly stoichiometric films although the amount of Co segregation in both S-poor and S-rich films is similar. Our findings on the influence of off-stoichiometry on the PMA and AHE are beneficial to design magnetic devices incorporated with the Weyl features of $\text{Co}_3\text{Sn}_2\text{S}_2$.

DOI: [10.1103/PhysRevMaterials.5.024403](https://doi.org/10.1103/PhysRevMaterials.5.024403)**I. INTRODUCTION**

The magnetic Weyl semimetal (WSM) is a class of quantum materials that host the relativistic Weyl node with an opposite chirality connected through the surface Fermi arc states [1–16]. Distinct physical properties in the WSMs have been well studied for a large intrinsic anomalous Hall effect (AHE) [8,10,11,17] and anomalous Nernst effect [18–20]. $\text{Co}_3\text{Sn}_2\text{S}_2$ shandite with a kagome lattice of Co [10,11,21–25], one of the representative examples for the WSM, is reported to exhibit a large AHE [10,11]. The AHE of bulk single crystals shows a tangent of the Hall angle reaching 0.2, far beyond that of conventional ferromagnetic transition metals and alloys [10,11], which is a hallmark of intrinsic feature of AHE originating from the large contribution of Berry curvature of Weyl nodes in the band structure [10,17]. The other distinct feature of $\text{Co}_3\text{Sn}_2\text{S}_2$ is a uniaxial magnetic anisotropy perpendicular to the Co-kagome layer [25,26]. The magnetic phases in $\text{Co}_3\text{Sn}_2\text{S}_2$ single crystals have been discussed with a complex spin texture owing to competition between the uniaxial magnetic anisotropy and the geometric frustration inherent to threefold symmetry of the kagome lattice [27,28].

In the case of c -axis oriented $\text{Co}_3\text{Sn}_2\text{S}_2$ thin films, the perpendicular magnetic anisotropy (PMA) can be obtained

as discussed later. The PMA in thin films is one of the key factors in the design of functional magnetic devices. The hard-magnet thin films with a perpendicular magnetic easy axis are beneficial for detection of magnetization direction and their capacity for high-density magnetic storage [29]. Therefore, the $\text{Co}_3\text{Sn}_2\text{S}_2$ thin films with PMA have potential for use in future magnetic and spintronics applications based on the Weyl features. However, the conventional mechanical exfoliation from the bulk single crystal is no longer feasible in $\text{Co}_3\text{Sn}_2\text{S}_2$ because of interlayer bonding along the c axis. Therefore, thin-film growth technique is one of the effective approaches to explore interesting magnetotransport phenomena stemming from the peculiar band topology of the WSMs in low dimensions or heterostructures [30,31]. Recently, growth of the c -axis oriented $\text{Co}_3\text{Sn}_2\text{S}_2$ thin films has been reported [32,33], showing the AHE with a large tangent of Hall angle comparable to the bulk value [32]. It has been also shown that the coercive field (H_c) of the perpendicular magnetization curve in the $\text{Co}_3\text{Sn}_2\text{S}_2$ film is much larger than that in bulk single crystal [32,33]. To discuss the large H_c accompanied with the Weyl features in thin films, the characterization and optimization of magnetic anisotropy, saturation magnetization (M_s), and AHE are essential in the $\text{Co}_3\text{Sn}_2\text{S}_x$ films with a wide range of chemical composition.

In this study, we investigated the magnetic anisotropy and AHE of $\text{Co}_3\text{Sn}_2\text{S}_x$ films for nearly stoichiometric, S-poor, and S-rich thin films fabricated by the cosputtering technique [32].

*junichi.shiogai@imr.tohoku.ac.jp

The PMA was discussed in terms of the effective perpendicular magnetic anisotropy constant K_u^{eff} , which was evaluated by comparing the magnetization hysteresis loops along the in-plane and out-of-plane directions. The AHE properties were characterized as a function of temperature and magnetic field. Finally, the magnetic anisotropy constant and the tangent of the Hall angle of all the films were compared with those of bulk single crystal.

II. EXPERIMENTAL DETAILS

40-nm-thick $\text{Co}_3\text{Sn}_2\text{S}_x$ films were prepared by radio-frequency magnetron sputtering on Al_2O_3 (0001) substrates. The targets, consisting of a SnS_n plate and Co metal chips, were cosputtered at substrate temperature of 400 °C. A 50- or 75-nm-thick SiO_x cap layer was then deposited and the samples were annealed at 800 °C. The composition ratio of Sn to Co was adjusted by the number and position of Co metal tips on the SnS_n plates while the ratio of S to Co was varied by different S compositions n in the SnS_n plates. The film thickness and the lattice parameters were characterized by their x-ray-diffraction (XRD) patterns, as reported in a previous paper [32]. The chemical composition ratios in the films were measured by energy-dispersive x-ray spectroscopy. The surface morphology was measured by atomic force microscope (Supplemental Material, Fig. S1 [34]). The magnetization of the $\text{Co}_3\text{Sn}_2\text{S}_x$ thin films was measured by magnetic property measurement system (Quantum Design Inc.) as a function of temperature and magnetic field applied parallel and perpendicular to the film plane. The longitudinal resistivity and Hall resistivity were measured by the dc five-point method in physical property measurement system (Quantum Design Inc.).

We obtained $\text{Co}_3\text{Sn}_2\text{S}_x$ thin films with nearly stoichiometric (sample A, $x = 2.02$), S-poor (sample B, $x = 1.54$), and S-rich (sample C, $x = 3.27$) compositions using the different sputtering targets with the SnS_n plate having $n = 1.35, 1.0,$ and $2.0,$ respectively, as summarized in Fig. 1(a) and Table I. The data of the $\text{Co}_3\text{Sn}_2\text{S}_x$ ($x = 2.2$) film fabricated using a $\text{SnS}_{1.5}$ plate in our previous study are also listed as a reference [32]. The obtained chemical compositions of Sn and S are compared as the ratio with respect to Co in Table I. For comparison, sample D was examined with the smaller Sn/Co and the slightly larger S/Co than stoichiometry in Supplemental Material, Table S1 and Fig. S2 [34]. As shown in Fig. 1(a), the S/Co composition ratio in the films is linearly dependent on n . The XRD patterns from the films were consistent with $\text{Co}_3\text{Sn}_2\text{S}_2$ (0003 m) peaks (not shown here) [32], indicating

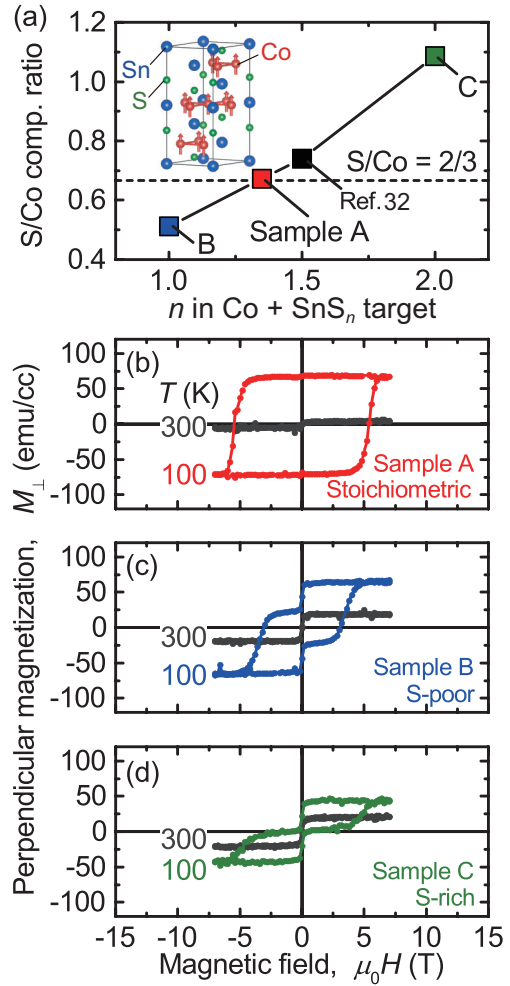


FIG. 1. (a) S/Co composition ratio of the $\text{Co}_3\text{Sn}_2\text{S}_x$ films as a function of chemical composition n of the sputtering targets SnS_n . The inset shows crystal structure of $\text{Co}_3\text{Sn}_2\text{S}_2$. A horizontal dashed line indicates the stoichiometric S/Co ratio. (b)–(d) Magnetic field dependences of magnetization at 100 K (red, blue, and green) and 300 K (gray) for (b) nearly stoichiometric sample A, (c) S-poor sample B, and (d) S-rich sample C, respectively. Here, the magnetic field is applied perpendicular to the film plane.

that the $\text{Co}_3\text{Sn}_2\text{S}_x$ films were grown with the c -axis orientation. In addition, S-poor sample B and S-rich sample C exhibit diffraction peaks from crystalline Co and a Sn-S compound, respectively. The c -axis lengths were estimated from the $\text{Co}_3\text{Sn}_2\text{S}_2$ (0006) diffraction peaks to be 1.316 nm for all the films (Table I), which is in good agreement with the bulk

TABLE I. A summary of the composition of the sputtering target, thickness (d), chemical composition ratio of Sn/Co and S/Co, c -axis length, and XRD intensity (I_{0006}) and full width of half maximum of the rocking curve ($\Delta\omega_{0006}$) of $\text{Co}_3\text{Sn}_2\text{S}_2$ (0006) peak for nearly stoichiometric sample A, S-poor sample B, S-rich sample C, and a reference reported previously [32].

	Target	d (nm)	Sn/Co	S/Co	c -axis length (nm)	I_{0006} (cps)	$\Delta\omega_{0006}$ (degree)
Sample A	Co + $\text{SnS}_{1.35}$	40	0.671	0.673	1.316	16242	0.0042
Sample B	Co + $\text{SnS}_{1.0}$	40	0.667	0.513	1.316	381	0.0573
Sample C	Co + $\text{SnS}_{2.0}$	40	0.629	1.09	1.316	37	0.0537
Ref. [32]	Co + $\text{SnS}_{1.5}$	35	0.676	0.741	1.316	8286	0.0036

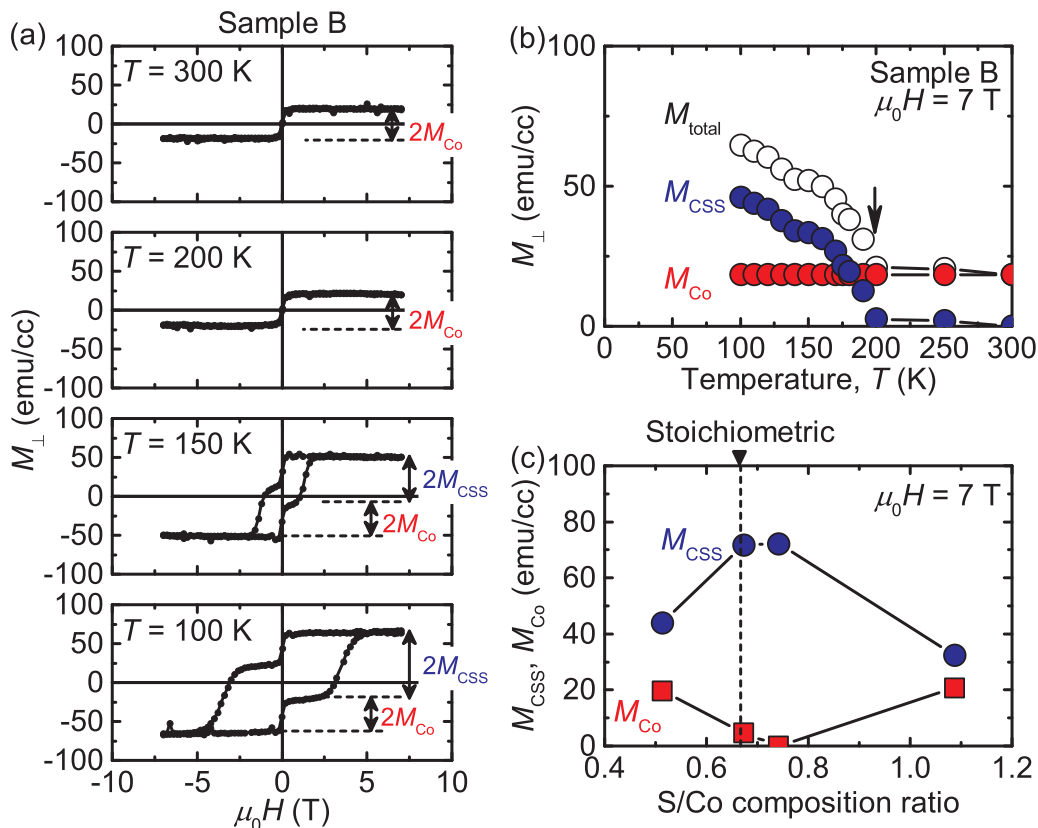


FIG. 2. (a) Magnetic field dependence of the magnetization of sample B measured at 300 (top panel), 200, 150, and 100 K (bottom panel). The field is applied perpendicular to the film plane. (b) Temperature dependence of the total magnetization extracted at 7 T (M_{total} , open circles), partial components of $\text{Co}_3\text{Sn}_2\text{S}_2$ (M_{CSS} , blue circles), and the Co metal (M_{Co} , red circles). Please see an explanation for the estimation method for M_{CSS} and M_{Co} in the text. (c) S/Co composition ratio dependences of M_{CSS} at 100 K and M_{Co} at 300 K. A vertical dashed line indicates the stoichiometric S/Co ratio.

value of 1.3178 nm (Joint Committee for Powder Diffraction Standards (JCPDS), PDF No. 01-0847267 and Ref. [23]). The independence of c -axis length on the S/Co ratio implies that the layered structure of the $\text{Co}_3\text{Sn}_2\text{S}_2$ is robust against off-stoichiometry. On the other hand, the peak intensity I_{0006} and full width at half maximum of the rocking curve $\Delta\omega_{0006}$ of $\text{Co}_3\text{Sn}_2\text{S}_2$ (0006) diffraction peak for S-poor sample B are inferior to that for nearly stoichiometric sample A by about two orders and one order of magnitude, respectively (Table I) [32]. Although the $\Delta\omega_{0006}$ of the S-rich sample C is comparable to that of sample B, the I_{0006} is much smaller by one order of magnitude, implying the crystallinity of the $\text{Co}_3\text{Sn}_2\text{S}_2$ phase in the S-rich film is the poorest among all three samples.

III. RESULTS AND DISCUSSION

Figure 1(b) shows the magnetic field ($\mu_0 H$, where μ_0 is the vacuum permeability) dependence of magnetization (M_{\perp} - H curve) for sample A under the field applied perpendicular to the plane at temperatures $T = 100$ K (red) and 300 K (gray). In this study, the M - H curves are mainly discussed above $T = 100$ K because the large H_c at lower temperature does not allow us to fully saturate the magnetization in the present apparatus, which has an upper limit of $\mu_0 H = 7$ T. At $T = 100$ K, a square-shaped hysteresis with a saturation magnetic field around 6 T is observed. This hysteresis loop

disappears at 300 K owing to the Curie temperature T_C of the nearly stoichiometric $\text{Co}_3\text{Sn}_2\text{S}_x$ ($x = 2.2$) film of around 180 K as reported previously [32]. On the other hand, a two-step feature is observed in the M_{\perp} - H curves of samples B and C at 100 K as shown in Figs. 1(c) and 1(d), respectively. Even at 300 K, the steplike component of M_{\perp} still remains [gray symbols in Figs. 1(c) and 1(d)]. This two-step feature is typically seen in materials with two coexisting magnetic components with different coercive fields and/or T_C . By comparing these M_{\perp} - H curves with sample A, the hysteresis component with a high saturation field around $\mu_0 H = 5$ -6 T was assigned to the magnetization of the $\text{Co}_3\text{Sn}_2\text{S}_2$ phase.

To further characterize these two components of magnetization, the M_{\perp} - H curves were measured at various temperatures. Figure 2(a) shows the M_{\perp} - H curves for the S-poor sample B at $T = 300$ (top panel), 200, 150, and 100 K (bottom panel). At 300 and 200 K, saturation magnetization M_s was comparable. At lower temperatures of 150 and 100 K, the two-step feature develops. These results indicate that the two-step M_{\perp} - H curve consists of two magnetization components with different T_C . In ferromagnetic substances constituted with Co, Sn, and/or S components, Co metal is the only ferromagnet, the T_C of which is higher than 300 K. Thus, the temperature-insensitive component corresponds to the magnetization of the segregated Co metal. It is important to note that the average size of the segregation is larger than roughly 0.4 nm (two atomic layers) of Co because the T_C of

the Co thin film is reduced to lower than room temperature when the thickness is thinner than two atomic layers due to the finite-size effect [35].

Each magnetization component of the $\text{Co}_3\text{Sn}_2\text{S}_2$ phase (denoted as M_{CSS} , blue solid circles), the Co phase (M_{Co} , red solid circles), and the total saturation magnetization of sample B (M_{total} , open circles) at 7 T are plotted as a function of T in Fig. 2(b). The M_{CSS} and M_{Co} values are extracted from the M_{\perp} - H curves as indicated by the arrows in Fig. 2(a). The temperature dependence of M_{total} reflects the superposition of temperature-insensitive M_{Co} (red) and the onset T_{C} at around 180 K of M_{CSS} (blue). The temperature-independent M_{Co} below $T = 300$ K evidences that this method is valid for quantitatively estimating the M_{CSS} in the off-stoichiometric films. The same analysis was applied to sample C in Supplemental Material, Fig. S3 [34]. Figure 2(c) summarizes S/Co composition ratio dependence of the M_{CSS} at 100 K and the M_{Co} at 300 K extracted by the method discussed above. The large M_{CSS} and the suppression of M_{Co} are simultaneously observed around the stoichiometric composition. Surprisingly, the detection of comparable M_{Co} in the S-poor and S-rich films indicates that the total amounts of the segregated magnetic Co in the films are comparable between them. In the S-poor sample, it is likely that the redundant Co is segregated. When we assume the room-temperature M_{s} of Co is 1446 emu/cc [36], volume fractions of the Co metal in samples B and C can be roughly estimated to be 1.4%. This result indicates that the Co metal is segregated in the S-rich sample C even though all the elements are enough supplied to form $\text{Co}_3\text{Sn}_2\text{S}_2$ phase. Note that the crystalline Co metal was not detected in the x-ray-diffraction pattern of sample C [32]. By applying identical analysis, the net volume fractions of $\text{Co}_3\text{Sn}_2\text{S}_2$ phase in samples B and C using the M_{s} of bulk (67 emu/cc) at 100 K [10] are estimated to be 65 and 48%, respectively. The rest of volume is composed of the segregated impurity phases such as the Co metal, and/or the Co-Sn, Co-S, Sn-S compounds, and the possible off-stoichiometric $\text{Co}_3\text{Sn}_2\text{S}_2$ phase. However, only Co and Sn_2S_3 were partially detected in the XRD pattern [32]. Although these estimations of the net volume fraction are helpful to consider the contained phases in the off-stoichiometric films, the M_{s} of $\text{Co}_3\text{Sn}_2\text{S}_2$ phase is likely different in each film. The connecting of the low M_{CSS} with the composition deficiency of $\text{Co}_3\text{Sn}_2\text{S}_2$ phase in samples B and C is quite difficult in this study. Further investigation using the microscopic structural characterization may be meaningful to determine the composition of segregations. In the following part, we discuss the magnetization of the $\text{Co}_3\text{Sn}_2\text{S}_2$ (M_{CSS}) by subtraction of the magnetization of the segregated Co at 300 K under the assumption of weak temperature dependence of the saturation magnetization of Co in the measurement temperatures.

Figure 3(a) shows the μ_0H dependence of M_{CSS} at 100 K for the field applied along out-of-plane (closed circles) and in-plane (open circles) directions for sample A. In contrast to the square-shaped out-of-plane M_{CSS} - H loop, the in-plane M_{CSS} - H loop shows almost the linear increase with μ_0H , which indicates that a magnetic hard axis is aligned in the plane. The anisotropic behavior is also obtained for sample B with a slightly smaller M_{s} as shown in Fig. 3(b). On the other hand, the in-plane and out-of-plane M_{CSS} - H loops match well

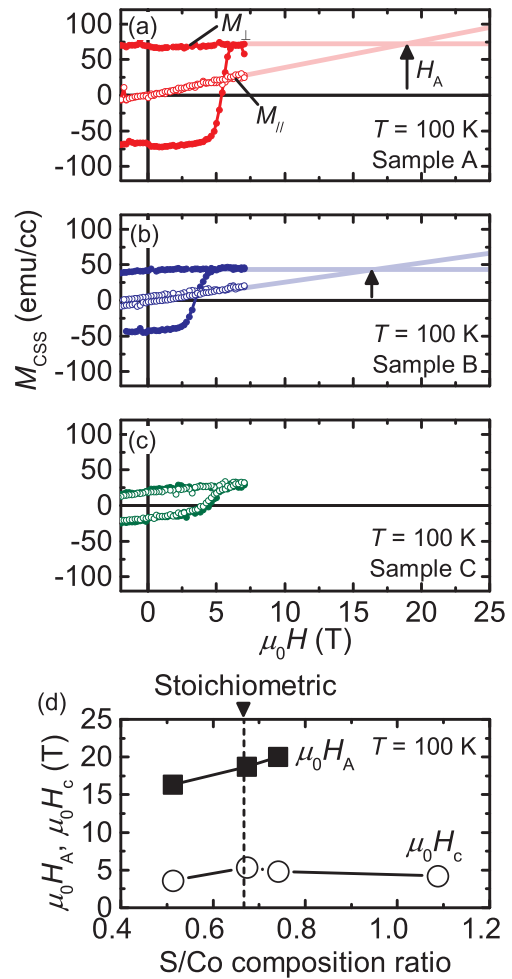


FIG. 3. (a)–(c) Magnetic field dependences of the magnetization component from $\text{Co}_3\text{Sn}_2\text{S}_2$ M_{CSS} at 100 K for (a) nearly stoichiometric sample A, (b) S-poor sample B, and (c) S-rich sample C, respectively. The field is applied along out-of-plane (M_{\perp} , closed) and in-plane (M_{\parallel} , open) directions. The M_{CSS} is obtained by subtracting magnetization at 300 K from that at 100 K. The bold lines indicate linear extrapolations to the higher field than our measurement limit of 7 T. The magnetic anisotropy field H_{A} is defined at the field where the two extrapolation lines from the out-of-plane and in-plane magnetization curves intersect. (d) S/Co composition ratio dependences of H_{A} (solid squares) and H_{c} (open circles) at 100 K with H_{c} being a coercive field. A vertical dashed line indicates the stoichiometric S/Co ratio.

for sample C as shown in Fig. 3(c), implying the isotropic feature. To characterize a magnetic anisotropy field H_{A} at 100 K within our measurement limit (7 T), we define the H_{A} as the magnetic field where linear extrapolations of the in-plane M_{CSS} - H curves reach the M_{s} , as indicated by black arrows in Figs. 3(a) and 3(b). Figure 3(d) summarizes the values of H_{A} as well as the coercive field H_{c} as a function of the S/Co composition ratio. Overall, the H_{A} is much larger than H_{c} in both samples A and B. The PMA is robustly maintained in the S-poor sample B, but the S-rich sample C exhibits isotropic properties. Considering the weak I_{0006} and large $\Delta\omega_{0006}$ for the S-rich sample C, the largely disordered stacking of Kagome layers induces the isotropic feature. Even though the

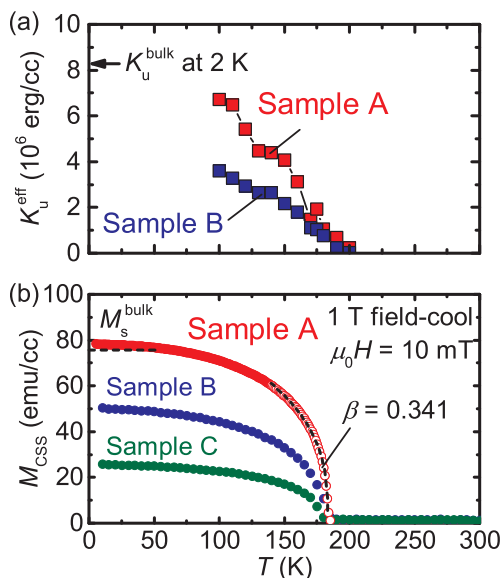


FIG. 4. (a) Temperature dependences of the effective perpendicular magnetic anisotropy constant K_u^{eff} for samples A (red squares) and B (blue squares). (b) Perpendicular magnetization as a function of temperature measured at 10 mT after field cooling at 1 T for samples A (red circles), B (blue circles), and C (green circles). Open circles indicate the data used for fitting. K_u^{bulk} and M_s^{bulk} indicate the bulk values at the lowest temperature reported in Ref. [26] and Ref. [10], respectively.

deficiency of sulfur is accommodated in the layered structure, it is likely that the redundant sulfur disturbs the formation of the Co-kagome layer and its stacking in the $\text{Co}_3\text{Sn}_2\text{S}_2$ structure. No XRD peaks from the planes of $\text{Co}_3\text{Sn}_2\text{S}_2$ other than $(0003m)$ were detected in sample C [32], elucidating that isotropic magnetization of sample C is not linked to the polycrystalline nature. The comparable values of H_c for all the films indicate that the magnetization reversal process is probably governed by the identical manner regardless of the defects in the films.

The effective perpendicular magnetic anisotropy constants K_u^{eff} of samples A and B can be evaluated by their anisotropic hysteresis loops using the following formula: $K_u^{\text{eff}} = \mu_0 H_A M_s / 2$. Figure 4(a) presents K_u^{eff} as a function of T for samples A (red squares) and B (blue squares). With decreasing T , the values of K_u^{eff} for both samples monotonically increase in the measurement temperature range to 6.7×10^6 erg/cm³ and 3.6×10^6 erg/cm³ at 100 K, respectively. The calculated K_u^{eff} value of sample B is only half that of sample A by using the total volume of the films, as shown in Fig. 4(a) due to the smaller M_s [Fig. 2(c)]. It is natural that the smaller K_u^{eff} for sample B than that for sample A agrees well with the smaller H_A in sample B discussed in Fig. 3. Although the K_u^{eff} values are comparable to the bulk value even at $T = 100$ K, the measurement of the K_u^{eff} values of the films at lower temperature by applying higher magnetic field is an interesting future task.

Figure 4(b) shows the T dependence of perpendicular magnetization for samples A (red), B (blue), and C (green) after field cooling at $\mu_0 H = 1$ T. The measurement was performed at $\mu_0 H = 10$ mT upon T increase. As discussed in

Figs. 3(a)–3(c) with out-of-plane and in-plane $M_{\text{CSS}}-H$ loops, the magnetization at 10 mT mainly corresponds to their saturation magnetization of M_{CSS} for samples A and B. Note that the M_{CSS} measured at 10 mT for sample C does not correspond to the saturation magnetization. While a clear onset magnetization is observed at around $T = 180$ K for all the samples, the saturation value of M_{CSS} is strongly dependent on the off-stoichiometry. The criticality around T_C is characterized by a critical exponent β as follows:

$$M \propto \left(1 - \frac{T}{T_C}\right)^\beta, \quad (2)$$

where the value of β depends on the dimensionality of the spontaneous magnetization. We discuss β value only for sample A because both magnetization and volume are accurately evaluated. The M_{CSS} in the other samples B and C may be underestimated due to the difficulty in estimation for the volume of the $\text{Co}_3\text{Sn}_2\text{S}_2$ phase in the films. By fitting the data around T_C with Eq. (2) [black dashed line in Fig. 4(b)], we obtained $\beta = 0.341$ (sample A), which is consistent with the bulk $\text{Co}_3\text{Sn}_2\text{S}_2$ [37]. In conventional discussions on the β value [38], $\beta = 0.341$ is close to the 3D XY model ($\beta = 0.345$), possibly being linked to the Co-kagome layered structure. A more careful analysis around T_C may be necessary to discuss magnetization scaling in kagome ferromagnet and contribution of the in-plane frustration [37,39]. The estimated T_C is weakly dependent on the off-stoichiometry at 183.4 K (sample A), 181.7 K (sample B), and 180.0 K (sample C). The value of M_{CSS} of sample A is comparable to that of the bulk single crystal [10], corresponding to $0.3 \mu_B$ per Co. In the case of samples B and C, the value of M_{CSS} is as small as approximately 64 and 32% of sample A, respectively, if we apply the total volume of the films. The squareness of $M_{\text{CSS}}-H$ in sample C is poor with respect to the other samples and its M_s is lowest as discussed in Fig. 2(c). We speculate the various origins for the smaller values of M_{CSS} in the S-poor sample B and in the S-rich sample C. In the ferromagnetism of $\text{Co}_3\text{Sn}_2\text{S}_2$ described by the Stoner model [40], the M_s value is correlated to the density of state (DOS) around the Fermi energy E_F . From the linear $\rho_{yx}-H$ curves in the paramagnetic state of $\text{Co}_3\text{Sn}_2\text{S}_2$ at 250 K, the Hall slope $\rho_{yx}/\mu_0 H$ corresponding to the carrier density varies from $+11.0 \times 10^{-3}$ cm³/C for sample A to $+6.11 \times 10^{-3}$ cm³/C for sample B, and $+0.71 \times 10^{-3}$ cm³/C for sample C, indicating an E_F shift by off-stoichiometry. While the reduction of the Hall slope does not directly reflect the increase or decrease of the carrier density in the semimetallic $\text{Co}_3\text{Sn}_2\text{S}_2$, the DOS at E_F of the $\text{Co}_3\text{Sn}_2\text{S}_2$ phase in the films is apparently different. Another possibility may be that the reduction of M_{CSS} results from the smaller volume fraction of the $\text{Co}_3\text{Sn}_2\text{S}_2$ phase in the off-stoichiometric samples. The comparable T_C for all three samples may mean that the obtained $\text{Co}_3\text{Sn}_2\text{S}_2$ phases in all films remain to be ferromagnetic while the volume fraction is possibly different as discussed in Fig. 2(c). We speculate that the ferromagnetism in the Co-kagome layer is robust even though the layer contains the excess Co, Sn, and/or sulfur deficiency.

The $M_{\text{CSS}}-H$ curves and the $\mu_0 H$ dependence of the Hall resistivity ρ_{yx} (Hall loop) at 100 K under a perpendicular H are

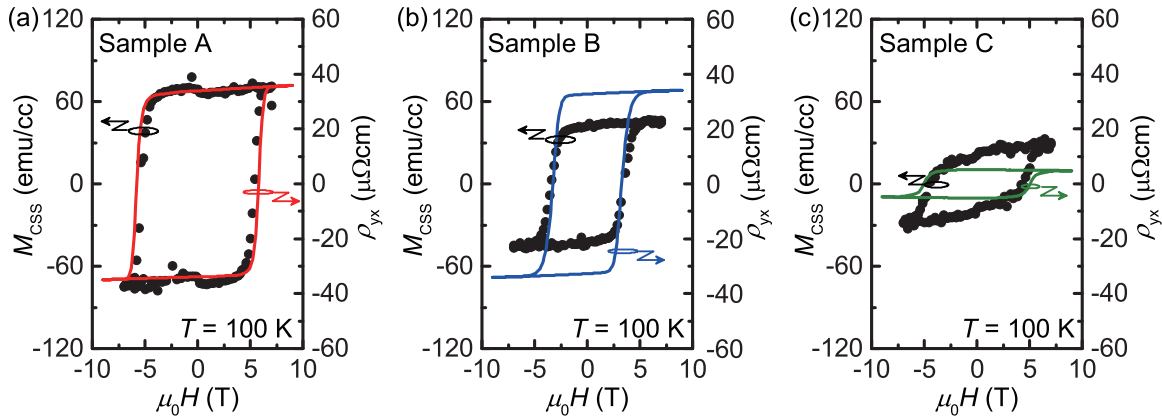


FIG. 5. (a)–(c) Perpendicular magnetic field dependences of the partial magnetization component from $\text{Co}_3\text{Sn}_2\text{S}_2$ (M_{CSS} , black circles in the left axis) and Hall resistivity (ρ_{yx} , colored line in the right axis) at 100 K for samples (a) A, (b) B, and (c) C, respectively.

shown for samples A, B, and C in Figs. 5(a)–5(c), respectively. The hysteresis loops of M_{CSS} and ρ_{yx} are in good agreement for all the samples, particularly in the H_c . The two-step feature is not observed in the ρ_{yx} - H curves, implying that the contribution of the segregated Co metal to the ρ_{yx} is negligible. The Hall conductivity of the Co metal was reported to be about 200 S/cm [41], which is one order of magnitude smaller than that of $\text{Co}_3\text{Sn}_2\text{S}_2$. In addition, the volume fraction of the Co segregation is as small as 1.4% as discussed in Fig. 2(c), consistent with the negligible contribution of Co to ρ_{yx} . The good agreement of H_c in M_{CSS} and ρ_{yx} proves that anomalous Hall resistivity is dominated by the $\text{Co}_3\text{Sn}_2\text{S}_2$ phase according to an empirical equation of $\rho_{yx} = R_0\mu_0H + R_A M_{\perp}$, where R_0 is the ordinary Hall coefficient, R_A the anomalous Hall coefficient, and M_{\perp} the perpendicular component of magnetization. In sample B, ρ_{yx} is rather large though the value of M_{CSS} is significantly lower than that of sample A, indicating that the value of R_A remains as large as that of sample A. However, both the M_{CSS} and ρ_{yx} values in sample C become significantly small. The AHE in $\text{Co}_3\text{Sn}_2\text{S}_2$ is mainly driven by the intrinsic mechanism, which originates from the contribution of the Weyl nodes [10,11]. The large contribution in the electronic bands mainly comes from Co-kagome layer [10]. Considering these trends in the values of M_{CSS} and ρ_{yx} , the Co-kagome layer of the $\text{Co}_3\text{Sn}_2\text{S}_2$ phase in the film would be severely damaged in the S-rich sample C.

The temperature dependences of electrical transport properties are discussed for each sample. The longitudinal resistivities ρ_{xx} of samples A (red), B (blue), and C (green solid line) are plotted as a function of temperature T in Fig. 6(a). The ferromagnetic transition appears as a clear hump observed for sample A corresponding to T_C [10,11]. The broader hump observed for the off-stoichiometric samples B and C may be linked to the deterioration of in-plane electrical conduction in the layered structure, i.e., the Co-kagome layer. In addition, the no systematic variation of ρ_{xx} among the three samples probably reflects a small contribution of the parasitic conduction from the other substances such as the segregated Co metal or the Co-Sn and Co-S composites in the films. As shown in Fig. 6(b), the Hall conductivity σ_{xy} rises at T_C of $\text{Co}_3\text{Sn}_2\text{S}_2$ phase as the anomalous Hall component starts to dominate. Here, σ_{xy} is calculated as $\sigma_{xy} = \rho_{yx}/(\rho_{xx}^2 + \rho_{yx}^2)$.

The rather large values of σ_{xy} for samples A and B at 10^3 S/cm are comparable to the value for the single crystals [10,11]. In contrast, the value of σ_{xy} for the S-rich sample C is significantly small while the comparable ρ_{xx} is observed in Fig. 6(a). The T dependences of the tangents of the Hall angle σ_{xy}/σ_{xx} are shown in Fig. 6(c). As observed in large σ_{xy} for both

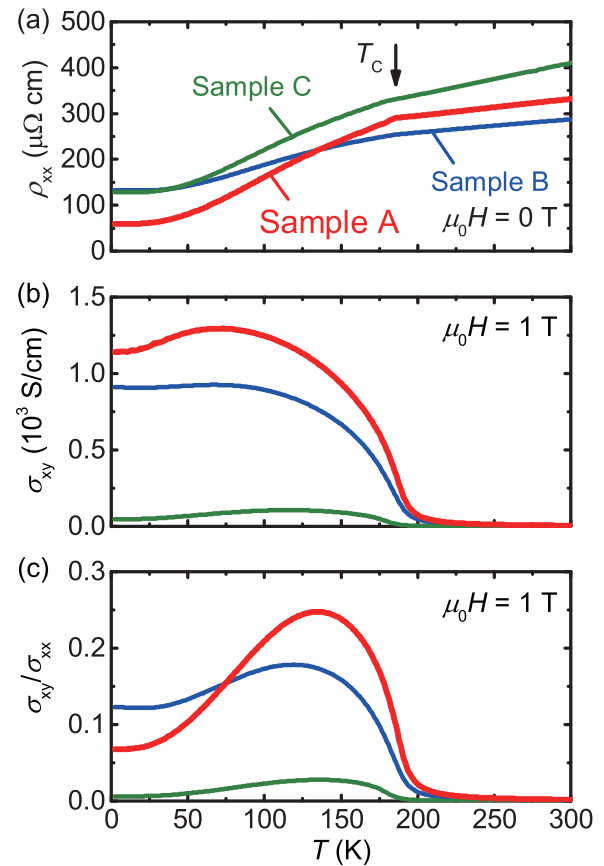


FIG. 6. (a)–(c) Temperature dependences of (a) longitudinal resistivity ρ_{xx} at 0 T, (b) Hall conductivity σ_{xy} measured at the perpendicular magnetic field of 1 T, and (c) tangent of Hall angle σ_{xy}/σ_{xx} at 1 T for samples A (red), B (blue), and C (green). The arrow in (a) indicates the hump in the ρ_{xx} - T curve of sample A.

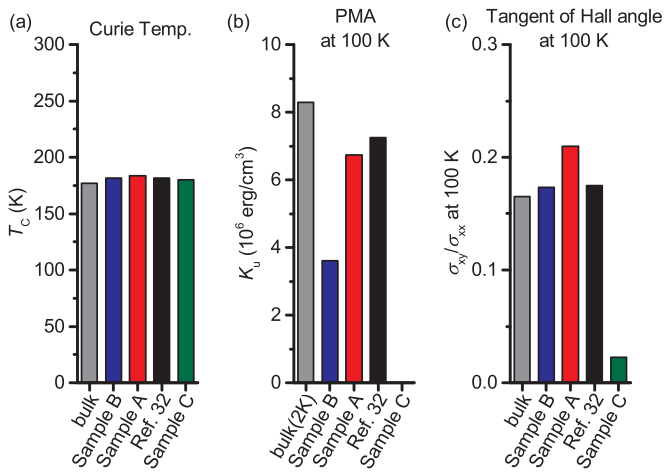


FIG. 7. (a)–(c) Summary of (a) ferromagnetic transition temperature (Curie temperature, T_C), (b) perpendicular magnetic anisotropy (PMA) constant, (c) tangent of Hall angle (σ_{xy}/σ_{xx}) for bulk single crystal (gray), S-poor sample B (blue), nearly stoichiometric sample A (red), a reference reported previously [32] (black), and S-rich sample C. In (b), the effective perpendicular magnetic anisotropy constants K_u^{eff} at 100 K are used for thin films and the uniaxial magnetic anisotropy constant at 2 K is used for bulk single crystal [26]. The values of T_C and σ_{xy}/σ_{xx} for the bulk are obtained from Ref. [10].

samples A and B, the T dependence of σ_{xy}/σ_{xx} shows the peak at around $T = 130$ K in the similar trend of bulk single crystal [10]. Indeed, the peak value of 0.25 in sample A reproduces the large value of 0.2 in bulk. Judging from these temperature dependences of σ_{xy} and σ_{xy}/σ_{xx} for sample A, the sample quality is high enough to discuss the Weyl features in view of AHE. In the case of sample C, the σ_{xy} is not activated by the deficiency of the Co-kagome layer as discussed in Fig. 5(c). The similar behavior was observed in the slightly S-rich sample D as discussed in Supplemental Material, Fig. S4 [34]. The slight difference of $\sigma_{xy}/\sigma_{xx}-T$ curves between samples A and B may be related to the E_F shift induced by the S deficiency.

Finally, we summarize T_C and magnetic anisotropy constant at $T = 100$ K, and the tangent of the Hall angle for the films and bulk single crystal [10,26]. The T_C of the $\text{Co}_3\text{Sn}_2\text{S}_x$ thin films are robust at around 180 K and independent of the S/Co composition ratio, as shown in Fig. 7(a). However, further study is required to determine the reason for the higher

T_C of off-stoichiometric samples than that of single crystals. In view of the PMA feature, the K_u^{eff} values at 100 K for the films and the uniaxial magnetic anisotropy constant at 2 K for the bulk single crystal [26] are compared in Fig. 7(b). The values of K_u^{eff} for the nearly stoichiometric sample A and the previous reference sample are much larger than that for the S-poor sample B. The K_u^{eff} value of the S-rich sample C is not plotted due to its isotropic $M_{\text{CSS}}-H$ loops. The K_u^{eff} value is not so large compared to well-investigated ferromagnetic metal thin films with a large PMA like FePt showing the value on the order of 10^7 erg/cc [42], because the M_s of $\text{Co}_3\text{Sn}_2\text{S}_2$ is smaller than that of those materials. In addition, we present the large value of σ_{xy}/σ_{xx} for samples A and B, and reference sample to reveal robustness of the AHE feature in the films. As clearly seen in Figs. 7(b) and 7(c), the asymmetric effect of off-stoichiometry on the PMA and AHE is observed in this study. Although the $\text{Co}_3\text{Sn}_2\text{S}_2$ phase in the S-rich sample C provides comparable T_C and ρ_{xx} , the anisotropic ferromagnetic character and the Weyl feature on AHE are drastically weakened. By contrast, the values of K_u^{eff} and σ_{xy}/σ_{xx} are maintained in the S-poor sample B while the segregation of the Co metal is comparable to that in the S-rich sample C. This suggests that the fine-tuning of the composition is critically important to observe Weyl features in the $\text{Co}_3\text{Sn}_2\text{S}_2$ thin films with PMA.

IV. CONCLUSION

We have performed the comprehensive study of thin films of the magnetic Weyl semimetal $\text{Co}_3\text{Sn}_2\text{S}_2$. The magnetic anisotropy and AHE were characterized for the 40-nm-thick thin films of $\text{Co}_3\text{Sn}_2\text{S}_x$ with different S compositions: $x = 2.02$ (stoichiometric), 1.54 (S poor), and 3.27 (S rich). A robust PMA and a large tangent of the Hall angle persist in the slightly S-poor film. On the other hand, the anisotropic property of the magnetization and the tangent of Hall angle are significantly inferior in the S-rich film. The fine-tuning of the sulfur composition into $2.0 < x < 2.2$ is critically important for capturing Weyl semimetallic features in sputtered $\text{Co}_3\text{Sn}_2\text{S}_x$ thin films. Our findings present an important insight for the device fabrication utilizing the interplay between ferromagnetism and topological electronic band.

ACKNOWLEDGMENTS

This work was partly supported by JSPS KAKENHI (Grants No. JP15H05853 and No. 18H05246) and JST CREST (Grant No. JPMJCR18T2).

[1] B. Yan and C. Felser, Topological materials: Weyl semimetal, *Annu. Rev. Condens. Matter Phys.* **8**, 337 (2017).
 [2] K. Manna, Y. Sun, L. Muechler, J. Kübler, and C. Felser, Heusler, Weyl and Berry, *Nat. Rev. Mater.* **3**, 244 (2018).
 [3] N. P. Armitage, E. J. Mele, and A. Vishwanath, Weyl and Dirac semimetals in three-dimensional solids, *Rev. Mod. Phys.* **90**, 015001 (2018).
 [4] X. Wang, A. M. Turner, A. Vishwanath, and S. Y. Savrasov, Topological semimetal and Fermi-arc surface states in the electronic structure of pyrochlore iridates, *Phys. Rev. B* **83**, 205101 (2011).

[5] A. A. Burkov and L. Balents, Weyl Semimetal in a Topological Insulator Multilayer, *Phys. Rev. Lett.* **107**, 127205 (2011).
 [6] G. Xu, H. Weng, Z. Wang, X. Dai, and Z. Fang, Chern Semimetal and the Quantized Anomalous Hall Effect in HgCr_2Se_4 , *Phys. Rev. Lett.* **107**, 186806 (2011).
 [7] Z. Wang, M. G. Vergniory, S. Kushwaha, M. Hirschberger, E. V. Chulkov, A. Ernst, N. P. Ong, R. J. Cava, and B. A. Bernevig, Time-Reversal-Breaking Weyl Fermions in Magnetic Heusler Alloys, *Phys. Rev. Lett.* **117**, 236401 (2016).
 [8] L. Ye, M. Kang, J. Liu, F. von Cube, C. R. Wicker, T. Suzuki, C. Jozwiak, A. Bostwick, E. Rotenberg, D. C. Bell *et al.*,

- Massive Dirac fermions in a ferromagnetic kagome metal, *Nature (London)* **555**, 638 (2018).
- [9] M. Kang, L. Ye, S. Fang, J.-S. You, A. Levitan, M. Han, J. I. Facio, C. Jozwiak, A. Bostwick, E. Rotenberg *et al.*, Dirac fermions and flat bands in the ideal kagome metal FeSn, *Nat. Mater.* **19**, 163 (2020).
- [10] E. Liu, Y. Sun, N. Kumar, L. Muechler, A. Sun, L. Jiao, S. Yang, D. Liu, A. Liang, Q. Xu *et al.*, Giant anomalous Hall effect in a ferromagnetic kagome-lattice semimetal, *Nat. Phys.* **14**, 1125 (2018).
- [11] Q. Wang, Y. Xu, R. Lou, Z. Liu, M. Li, Y. Huang, D. Shen, H. Weng, S. Wang, and H. Lei, Large intrinsic anomalous Hall effect in half-metallic ferromagnet $\text{Co}_3\text{Sn}_2\text{S}_2$ with magnetic Weyl fermions, *Nat. Commun.* **9**, 3681 (2018).
- [12] G. Chang, S. Xu, H. Zheng, B. Singh, C. Hsu, G. Bian, N. Alidoust, I. Belopolski, D. S. Sanchez, S. Zhang *et al.*, Room-temperature magnetic topological Weyl fermion and nodal line semimetal states in half-metallic Heusler Co_2TiX ($X = \text{Si, Ge, or Sn}$), *Sci. Rep.* **6**, 38839 (2016).
- [13] J. Kubler and C. Felser, Weyl points in the ferromagnetic Heusler compound Co_2MnAl , *EPL* **114**, 47005 (2016).
- [14] I. Belopolsky, K. Manna, D. S. Sanchez, G. Chang, B. Ernst, J. Yin, S. S. Zhang, T. Cochran, N. Shumiya, H. Zheng *et al.*, Discovery of topological Weyl fermion lines and drum-head surface states in a room temperature magnet, *Science* **365**, 1278 (2019).
- [15] D. F. Liu, A. J. Liang, E. K. Liu, Q. N. Xu, Y. W. Li, C. Chen, D. Pei, W. J. Shi, S. K. Mo, P. Dudin *et al.*, Magnetic Weyl semimetal phase in a Kagomé crystal, *Science* **365**, 1282 (2019).
- [16] N. Morali, R. Batabyal, P. K. Nag, E. Liu, Q. Xu, Y. Sun, B. Yan, C. Felser, N. Avraham, H. Beidenkopf *et al.*, Fermi-arc diversity on surface terminations of the magnetic Weyl semimetal $\text{Co}_3\text{Sn}_2\text{S}_2$, *Science* **365**, 1286 (2019).
- [17] N. Nagaosa, J. Sinova, S. Onoda, A. H. MacDonald, and N. P. Ong, Anomalous Hall effect, *Rev. Mod. Phys.* **82**, 1539 (2010).
- [18] S. N. Guin, P. Vir, Y. Zhang, N. Kumar, S. J. Watzman, C. Fu, E. Liu, K. Manna, W. Schnelle, J. Gooth *et al.*, Zero-field Nernst effect in a ferromagnetic kagome-lattice Weyl-semimetal $\text{Co}_3\text{Sn}_2\text{S}_2$, *Adv. Mater.* **31**, 1806622 (2019).
- [19] A. Sakai, Y. P. Mizuta, A. A. Nugroho, R. Sihombing, T. Koretsune, M. Suzuki, N. Takemori, R. Ishii, D. Nishio-Hamane, R. Arita *et al.*, Giant anomalous Nernst effect and quantum-critical scaling in a ferromagnetic semimetal, *Nat. Phys.* **14**, 1119 (2018).
- [20] S. N. Guin, K. Manna, J. Noky, S. J. Watzman, C. Fu, N. Kumar, W. Schnelle, C. Shekhar, Y. Sun, J. Gooth, and C. Felser, Anomalous Nernst effect beyond the magnetization scaling relation in the ferromagnetic Heusler compound Co_2MnGa , *NPG Asia Mater.* **11**, 16 (2019).
- [21] S. Natarajan, G. V. Subba Rao, R. Baskaran, and T. S. Radhakrishnan, Synthesis and electrical properties of shandite-parkerite phases, $\text{A}_2\text{M}_3\text{Ch}_2$, *J. Less-Common Met.* **138**, 215 (1988).
- [22] M. Holder, Y. S. Dedkov, A. Kade, H. Rosner, W. Schnelle, A. Leithe-Jasper, R. Wehrich, and S. L. Molodtsov, Photoemission study of electronic structure of the half-metallic ferromagnet $\text{Co}_3\text{Sn}_2\text{S}_2$, *Phys. Rev. B* **79**, 205116 (2009).
- [23] W. Schnelle, A. Leithe-Jasper, H. Rosner, F. M. Schappacher, R. Pöttgen, F. Pielhofer, and R. Wehrich, Ferromagnetic ordering and half-metallic state of $\text{Sn}_2\text{Co}_3\text{S}_2$ with the shandite-type structure, *Phys. Rev. B* **88**, 144404 (2013).
- [24] Y. Sakai, R. Tanakadate, M. Matoba, I. Yamada, N. Nishiyama, T. Irifune, K. Funakoshi, T. Kunimoto, Y. Higo, and Y. Kamihara, Magnetic properties of shandite-phase $\text{Co}_{3-x}\text{Fe}_x\text{Sn}_2\text{S}_2$ ($x = 0-1.0$) obtained with high pressure synthesis, *J. Phys. Soc. Jpn.* **84**, 044705 (2015).
- [25] M. A. Kassem, Y. Tabata, T. Waki, and H. Nakamura, Quasi-two-dimensional magnetism in Co-based shandites, *J. Phys. Soc. Jpn.* **85**, 064706 (2016).
- [26] J. Shen, Q. Zeng, S. Zhang, W. Tong, L. Ling, C. Xi, Z. Wang, E. Liu, W. Wang, G. Wu, and B. Shen, On the anisotropies of magnetization and electronic transport of magnetic Weyl semimetal $\text{Co}_3\text{Sn}_2\text{S}_2$, *Appl. Phys. Lett.* **115**, 212403 (2019).
- [27] M. A. Kassem, Y. Tabata, T. Waki, and H. Nakamura, Low-field anomalous magnetic phase in the kagome-lattice shandite $\text{Co}_3\text{Sn}_2\text{S}_2$, *Phys. Rev. B* **96**, 014429 (2017).
- [28] Z. Guguchia, J. A. T. Verezhak, D. J. Gawryluk, S. S. Tsirkin, J.-X. Yin, I. Belopolski, H. Zhou, G. Simutis, S.-S. Zhang, T. A. Cochran *et al.*, Tunable anomalous Hall conductivity through volume-wise magnetic competition in a topological kagome magnet, *Nat. Commun.* **11**, 559 (2020).
- [29] A. Brataas, A. D. Kent, and H. Ohno, Current-induced torques in magnetic materials, *Nat. Mater.* **11**, 372 (2012).
- [30] L. Muechler, E. Liu, J. Gayles, Q. Xu, C. Felser, and Y. Sun, Emerging chiral edge states from the confinement of a magnetic Weyl semimetal in $\text{Co}_3\text{Sn}_2\text{S}_2$, *Phys. Rev. B* **101**, 115106 (2020).
- [31] D. Kurebayashi and K. Nomura, Voltage-Driven Magnetization Switching and Spin Pumping in Weyl Semimetals, *Phys. Rev. Appl.* **6**, 044013 (2016).
- [32] K. Fujiwara, J. Ikeda, J. Shiogai, T. Seki, K. Takanashi, and A. Tsukazaki, Ferromagnetic $\text{Co}_3\text{Sn}_2\text{S}_2$ thin films fabricated by co-sputtering, *Jpn. J. Appl. Phys.* **58**, 050912 (2019).
- [33] S. Li, G. Gu, E. Liu, P. Cheng, B. Feng, Y. Li, L. Chen, and K. Wu, Epitaxial growth and transport properties of magnetic Weyl semimetal $\text{Co}_3\text{Sn}_2\text{S}_2$ thin films, *ACS Appl. Electron. Mater.* **2**, 126 (2020).
- [34] See Supplemental Material at <http://link.aps.org/supplemental/10.1103/PhysRevMaterials.5.024403> for atomic force micrograph of surface morphology of the samples, magnetization, and transport properties of sample D with the different S/Co and Sn/Co composition.
- [35] C. M. Schneider, P. Bressler, P. Schuster, J. Kirschner, J. J. de Miguel, and R. Miranda, Curie Temperature of Ultrathin Films of fcc-Cobalt Epitaxially Grown on Atomically Flat Cu(100) Surfaces, *Phys. Rev. Lett.* **64**, 1059 (1990).
- [36] E. P. Wohlfarth, in *Ferromagnetic Materials: A Handbook of the Properties of magnetically Ordered Substances*, edited by E. P. Wohlfarth (North-Holland, Amsterdam, 1980), Vol. 1, p. 20.
- [37] W. Yan, X. Zhang, Q. Shi, X. Yu, Z. Zhang, Q. Wang, Si Li, and H. Lei, Critical behavior of half-metallic ferromagnet $\text{Co}_3\text{Sn}_2\text{S}_2$, *Solid State Commun.* **281**, 57 (2018).
- [38] H. E. Stanley, in *Introduction to Phase Transitions and Critical Phenomena* (Oxford University Press, Oxford, 1871).

- [39] M. A. Kassem, Y. Tabata, T. Waki, and H. Nakamura, Unconventional critical behaviors at the magnetic phase transition of $\text{Co}_3\text{Sn}_2\text{S}_2$ kagome ferromagnet, *J. Phys.: Condens. Matter* **33**, 015801 (2020).
- [40] A. Ozawa and K. Nomura, Two-orbital effective model for magnetic Weyl semimetal in kagome-lattice shandite, *J. Phys. Soc. Jpn.* **88**, 123703 (2019).
- [41] J. Kötzler and W. Gil, Anomalous Hall resistivity of cobalt films: Evidence for the intrinsic spin-orbit effect, *Phys. Rev. B* **72**, 060412(R) (2005).
- [42] M. R. Visokay and R. Sinclair, Direct formation of ordered CoPt and FePt compound thin films by sputtering, *Appl. Phys. Lett.* **66**, 1692 (1995).